Lab on a Chip

PAPER

View Article Online
View Journal | View Issue

Cite this: *Lab Chip*, 2022, **22**, 2315

Systematic characterization of effect of flow rates and buffer compositions on double emulsion droplet volumes and stability†

Suzanne G. K. Calhoun,[a] Kara K. Brower,[bc] Vineeth Chandran Suja,[ad] Gaeun Kim,[b] Ningning Wang,[e] Alexandra L. McCully,[f] Halim Kusumaatmaja,[g] Gerald G. Fuller[a] and Polly M. Fordyce *[bchi]

Double emulsion droplets (DEs) are water/oil/water droplets that can be sorted *via* fluorescence-activated cell sorting (FACS), allowing for new opportunities in high-throughput cellular analysis, enzymatic screening, and synthetic biology. These applications require stable, uniform droplets with predictable microreactor volumes. However, predicting DE droplet size, shell thickness, and stability as a function of flow rate has remained challenging for monodisperse single core droplets and those containing biologically-relevant buffers, which influence bulk and interfacial properties. As a result, developing novel DE-based bioassays has typically required extensive initial optimization of flow rates to find conditions that produce stable droplets of the desired size and shell thickness. To address this challenge, we conducted systematic size parameterization quantifying how differences in flow rates and buffer properties (viscosity and interfacial tension at water/oil interfaces) alter droplet size and stability, across 6 inner aqueous buffers used across applications such as cellular lysis, microbial growth, and drug delivery, quantifying the size and shell thickness of >22 000 droplets overall. We restricted our study to stable single core droplets generated in a 2-step dripping–dripping formation regime in a straightforward PDMS device. Using data from 138 unique conditions (flow rates and buffer composition), we also demonstrated that a recent physically-derived size law of Wang *et al.* can accurately predict double emulsion shell thickness for >95% of observations. Finally, we validated the utility of this size law by using it to accurately predict droplet sizes for a novel bioassay that requires encapsulating growth media for bacteria in droplets. This work has the potential to enable new screening-based biological applications by simplifying novel DE bioassay development.

Received 11th March 2022,
Accepted 3rd May 2022

DOI: 10.1039/d2lc00229a

rsc.li/loc

Introduction

In the past ten years, droplet microfluidic techniques have enabled new biological assays at unprecedented scale with applications ranging from disease diagnosis[2–4] to synthetic biology[5–9] and single cell analysis.[10–14] Double emulsion (DE) (W/O/W water/oil/water) droplets are of particular interest, as their unique architecture allows them to be used as biological microreactors in drug delivery and synthetic cell engineering and to be sorted according to fluorescence using common fluorescence-activated cell sorting (FACS) instruments.[15–17] This ability to sort DEs in high-throughput unlocks new opportunities for cellular screening (*e.g.* live-cell secretomics, next-generation sequencing of rare populations, and multiomic single cell analysis).[12,18–20]

However, DE droplets are generally considered more challenging to produce than single emulsion (SE) droplets. Each DE droplet contains a double layer structure comprised of an inner aqueous core encapsulated within an outer oil

[a] *Department of Chemical Engineering, Stanford University, Stanford, CA 94305, USA*
[b] *Department of Bioengineering, Stanford University, Stanford, CA 94305, USA. E-mail: pfordyce@stanford.edu*
[c] *ChEM-H Institute, Stanford University, Stanford, CA 94305, USA*
[d] *School of Engineering and Applied Sciences, Harvard University, MA – 01234, USA*
[e] *School of Energy & Power Engineering, Xi'an Jiaotong University, Xi'an 710049, China*
[f] *Department of Civil & Environmental Engineering, Stanford University, Stanford, CA 94305, USA*
[g] *Department of Physics, Durham University, Durham DH1 3LE, UK*
[h] *Department of Genetics, Stanford University, Stanford, CA 94305, USA*
[i] *Chan Zuckerberg BioHub, San Francisco, CA 94158, USA*

† Electronic supplementary information (ESI) available. See DOI: https://doi.org/10.1039/d2lc00229a

droplet that is in turn within an aqueous outer buffer.[16,21,22] DE droplet stability and shell thickness therefore require balancing multiple inertial, capillary, viscous and shear forces that arise at two different interfaces during droplet generation, reaction processing and flow cytometry.[1,23–25] Further complicating assay development, even small changes in inner aqueous buffer composition can change physical fluid properties and alter this balance of forces.[1,26]

Altered diameters of DE droplet inner cores and oil shells can dramatically impact downstream biological assays.[14,16,27,28] Small differences in inner aqueous core volume can lead to large changes in diffusion kinetics and surface area-to-volume ratio,[4,29,30] thereby modifying effective soluble concentrations of proteins, enzymes, and reagents. In cell encapsulation assays, changes to the inner aqueous core volume can also alter the loading distribution of cells within droplets.[16,31,32] Beyond the inner aqueous core, efficient screening, sorting, and recovery of DE droplets *via* FACS depends on both overall droplet volume and the thickness and deformability of the oil shell.[16,33,34] Successful clog-free FACS requires single core, uniform DE droplets.[4,16,30,33,35–37] Furthermore, recent computational work suggests that high deformability, imparted by specific surfactants and thin oil shells, facilitates robust FACS by allowing droplets to flex in response to strong shear forces in the nozzle.[15,33,38,39] Thin shells also hinder coalescence by increasing hydrodynamic resistance, which decreases core mobility and causes very thin shells to act as a lubricant.[15,38,40]

DE droplet generation *via* microfluidic devices[41,42] provides improved control of size and monodispersity compared with traditional methods like bulk emulsification.[43] In most cases, DEs are generated *via* a one-step formation regime in which three flow rates must be balanced at one pinch-off point as inner and outer droplets shear simultaneously, as in single emulsion reinjection devices[43–45] or glass coaxial capillary devices,[41,43,46] but these approaches require technical skill to operate and can increase polydispersity.[1,17,41,43,47] As an alternate approach, PDMS devices that generate DEs *via* a two-step flow regime, with distinct pinch-off points for the inner and outer droplets on a single device,[1] create single core monodisperse droplets ideal for FACS and are straightforward to operate, requiring precise balancing of only two flow rates simultaneously.

Currently, it is difficult or impossible to predict the flow rates required to produce DE droplets with a desired size and shell thickness *via* two-step formation with certain solution compositions, largely due to a lack of systematic and quantitative characterization data. Several prior experimental studies have explored the effect of flow rates[48–51] and device geometry[52–54] on DE size and shell thickness in one-step formation, while other studies have focused on multicore or 3+ layer emulsions for designer particles,[17,27,41,46,51,55–58] yet droplet size in two-step formation has not been well characterized beyond T junctions[59] and transitions between one- and two-step formation.[27,60] Moreover, experimental studies have been limited to idealized flow solutions (*e.g.* PEG–dextran or PBS) and have not focused on single core droplets, doubly limiting translation to biological assays. Numerical studies of one-step formation systems have addressed the importance of flow rates, interfacial tension, geometry,[61,62] viscosity,[63] and flow regime prediction,[54] and have formulated size scaling laws,[40,41,64] yet few systematic experimental studies have been conducted to validate these proposed size laws and stability regimes. A systematic understanding of how flow rates and solution composition impact DE droplet size, shell thickness, and stability in two-step formation devices could therefore greatly simplify initial assay development.

We previously developed an open-source device design (Dropception) and workflow for robustly generating and sorting DE droplets *via* FACS.[16] Here, we build on this work with a systematic scan of DE droplet size across a wide range of different buffer solutions and flow rates, with a particular focus on varying the inner aqueous buffer, most likely to change between biological assays. By restricting our work to a stable dripping–dripping flow regime with matched periodicity in a two-step formation device, we focused our investigation exclusively on regimes that produce the single-core droplets essential to FACS. Overall, we quantified size and shell thickness for DE droplets containing 6 different inner aqueous buffers as a function of 138 combinations of aqueous inner and oil flow rates that yielded monodisperse single core DE droplet populations with $<5\%$ CV in size. In parallel, we characterized bulk and interfacial properties of each aqueous input solution to understand how interfacial tension and viscosity influence droplet size and stability. We applied a recent size scaling model of one-step formation by Wang *et al.*[1] to our two-step formation regime and systematic dataset, empirically validating this model for many biological applications. To test the accuracy of the model, we predicted droplet flow rates for desired shell thickness with a novel inner aqueous buffer, generated droplets, and confirmed that measured droplet size matched predictions. We anticipate that this platform, model and data will prove broadly useful for life scientists seeking to develop new DE-based assays.

Results and discussion

1. Size characterization pipeline

To develop a generalizable and predictive model for DE droplet size and shell thickness as a function of flow rate, we: (1) generated stable single core DE droplets under varying flow rates and incorporating different buffers and surfactants, (2) quantified droplet size and shell thickness *via* microscopy, and (3) used these data to derive fit parameters for a universal size scaling law that predicts droplet size and shell thickness using only flow rates and surfactant properties as inputs (Fig. 1).

2. Double emulsion droplet generation *via* dripping–dripping regime

We generated DE droplets using an integrated single-layer microfluidic device ('Dropception') that forms both the core

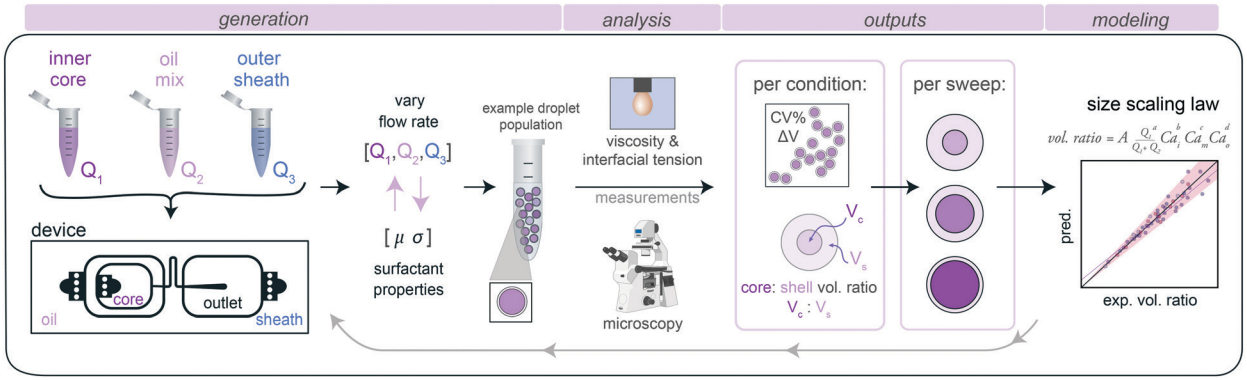

Fig. 1 DE size characterization pipeline: (1) generation of W/O/W droplets from different inner aqueous buffers, oil mix, and outer sheath buffer across multiple flow rate conditions, (2) analysis to quantify droplet size and shell thickness *via* microscopy, with outputs of % CV and core : shell volume ratio of each condition, and viscosity and interfacial tension (IFT) *via* pendant drop tensiometry and cone and plate rheometry, and (3) modeling to derive a universal scaling law capable of predicting droplet shell thickness from flow rates and IFTs.

W/O droplet and final W/O/W droplet on the same chip.[16,31] DE droplets are formed *via* a dual flow focuser geometry: single aqueous buffer-in-oil droplets are formed at the first flow focusing junction (FF1), and then these droplets are encapsulated within an oil shell *via* pinch-off of the W/O droplet in a fast-flowing outer aqueous sheath solution stream at the second flow focusing junction (FF2).

Between FF1 and FF2 (FF1: 22.5 μm wide × 22.5 μm tall, FF2: 50 μm × 50 μm), a serpentine flow resistor (22.5 μm wide × 22.5 μm tall) increases resistance to equally space W/O droplets prior to pinch-off (Fig. 1 and S1†). At FF2, the channel height increases to 50 μm, which reduces downstream resistance to create a dominant dripping–dripping regime for droplet formation (Movie S1†) and prevent the jetting–dripping droplet formation previously seen in DE generation systems.[1,27] In this scheme, FF1 and FF2 function as largely decoupled systems, allowing us to hold outer sheath flow rates (Q_3) constant and generate DEs with a constant outer diameter for reproducible FACS sorting while varying inner aqueous (Q_1) and oil (Q_2) rates to alter inner droplet size. The device geometry of a flow resistor separating the two flow focusers effectively eliminates possibility of several unstable flow regimes, making stable droplets more easily achievable.

This device reduces size variability associated with the reinjection required for two-step droplet generation, is easy to fabricate, and requires only 3 syringe pumps for operation (<$10 000 total cost). While the Dropception device used here produces droplets of total diameter ~40 μm (sortable with FACS), it can be globally scaled to produce smaller or larger DEs.

3. Size parameterization flow rate sweep: base condition

Using this device, we designed a systematic size parameterization sweep to test how varying flow rates altered DE droplet size and shell thickness. Here we sequentially vary Q_1 and Q_2 (inner and oil flow rates) while holding Q_3 constant to decrease number of variables. To systematically sample stable flow rate conditions, we varied either: (1) Q_1 alone while keeping Q_2 constant, (2) Q_2 alone while keeping Q_1 constant, or (3) both Q_1 and Q_2 simultaneously while keeping their total flow rate constant ($Q_t = Q_1 + Q_2$) (Fig. S2†).

To provide high-resolution information at flow rates most likely to be useful for biologists interested in sorting DEs, we first identified a central condition that generated stable single core droplets with a core : shell ratio of ~0.60 and then sampled the stable range in regularly spaced intervals in either direction. At edges of the sample ranges, single core droplets gave way to other behaviours (*e.g.* droplets with multiple cores, droplets with satellite oil drops, and droplets without cores) (Fig. S2†). We define a stable flow rate condition as a dripping–dripping flow regime with matching periodicity of SE formation at FF1 with DE encapsulation at FF2 that produces droplets with >95% single cores as determined by microscopy; we considered any formation behaviour outside these restrictions an instability.

To begin, we tested DEs composed of solutions previously optimized for FACS:[16] (1) an inner aqueous buffer typically used for protein extraction, gentle cell lysis, and ddPCR droplet applications (1X PBS and 1% Tween-20, a polysorbate-family nonionic detergent), (2) an oil solution, consisting of HFE 7500 fluorinated oil with 2.2% Ionic Krytox FSH-157 surfactant, that is biocompatible and frequently used in cell growth and droplet PCR applications,[4,16] and (3) an outer aqueous sheath solution comprised of 1X PBS with 2% Pluronic F68 and 1% Tween-20. For this droplet composition, a wide range of flow rates (Q_1: 110–230 μl h^{-1}, Q_2: 280–760 μl h^{-1}) produced highly monodisperse single core droplets with core volume : shell volume ratios ($V_c : V_s$) from 0.181–0.703 (Fig. 2A and B; Table S5†). As expected, reducing the inner aqueous flow rate (Q_1) linearly decreased core volume (Fig. 2B, middle), increasing the oil flow rate (Q_2) linearly increased shell thickness (Fig. 2B, left), and changing Q_1 and Q_2 simultaneously while maintaining the same total inner flow rate (Q_t) generated droplets with a constant outer diameter (Fig. 2B). Surprisingly, varying either Q_1 or Q_2 while keeping the other inner flow rate constant

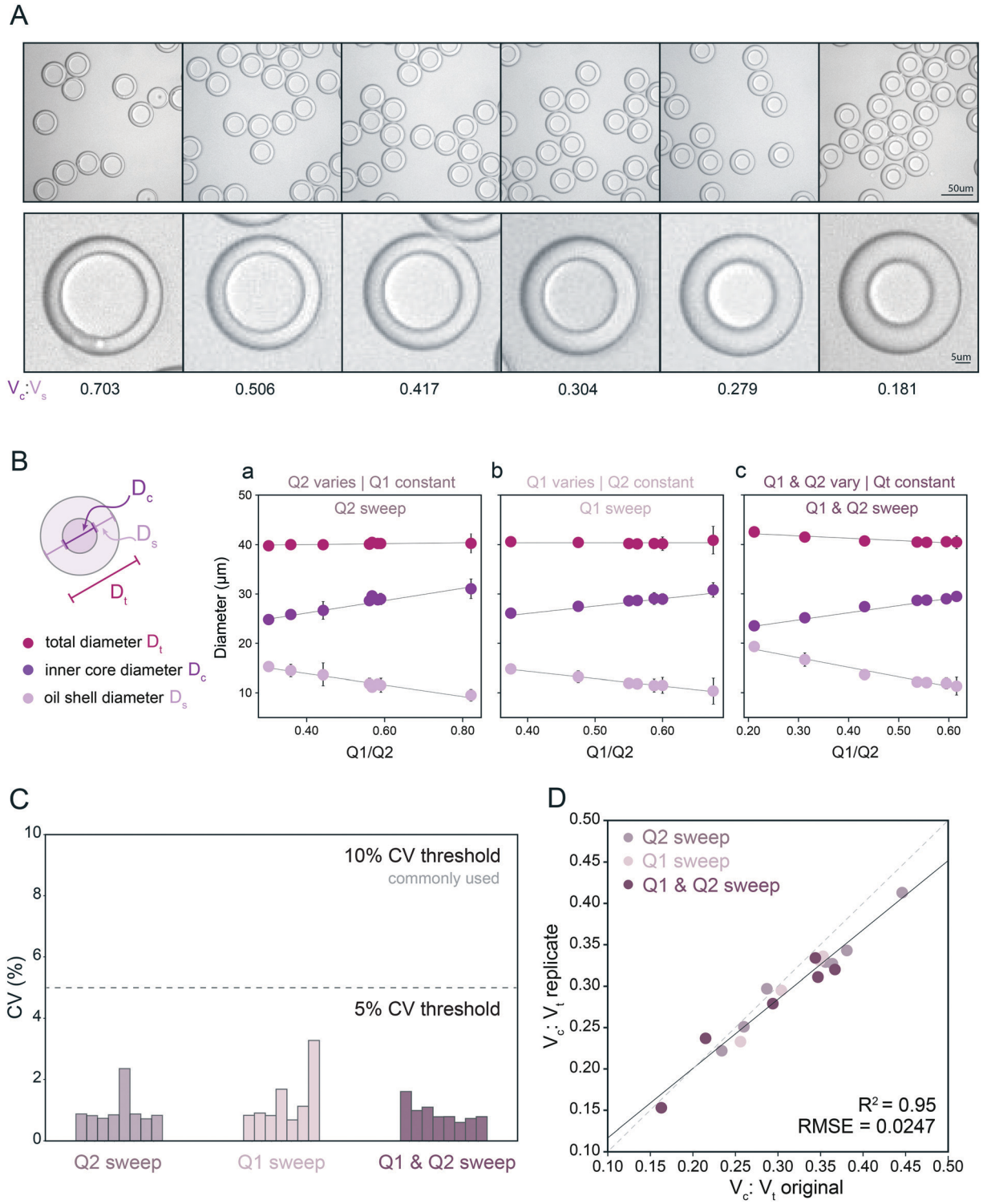

Fig. 2 Measured droplet diameters as a function of flow rates for droplets containing PBS + 1% Tween-20. (A) Representative bright field microscopy images of monodisperse DE droplets across varying core: shell volume ratios. (B) Measured total diameters (magenta markers), oil shell diameters (lavender markers), and inner core diameters (purple markers) for flow conditions varying oil flow rate (Q_2) only (left), inner aqueous flow rate (Q_1) only (middle), or simultaneously varying Q_1 and Q_2 (right). Markers indicate mean, error bars represent standard deviation, and solid lines show a linear regression. (C) Measured diameter coefficient of variation (CV) (%); see Table S5† for number of droplets for each flow condition. (D) Measured core: total volume ratios across 2 replicates for all flow conditions (see Table S5† for number of droplets per condition). Dashed line indicates 1 : 1 relationship, solid line indicates linear regression.

generated droplets with a largely constant outer diameter (mean: 39.4 μm) despite large changes in Q_t. This is consistent with the device's flow resistor shielding FF2 from most effects of FF1 variation at constant Q_3 under the requirement of matched single emulsion and double emulsion encapsulation rates at FF1 and FF2. The dynamic range of the oil flow rate (Q_2) that generated monodisperse droplets was wider than that for inner aqueous flow rate (Q_1), consistent with the lower viscosity and interfacial tension (IFT) of the oil solution (global statistics, Table 1; fluid properties, Table 2; ranges, Table S5†). Overall, the mean CVs for all measured outer diameters and inner core diameters were 2.16% and 1.51%, respectively, with all combinations under the 5% CV line, important for reaction success and large particle FACS, highly sensitive to clogs (Fig. 2C).[16,45,65]

To test reproducibility of measured rates for these solutions and device geometry, we repeated all measurements using a new Dropception device in a different laboratory (Fig. S3†). Measured diameters showed strong agreement across replicates (Fig. 2D, R^2, residual norm. = 95%, 0.0247), demonstrating the ability to reliably use flow rates to specify aqueous core reactor diameters from 21.9–29.4 μm and overall droplet diameters from 38.6–41.0 μm for this surfactant formulation and device design. While most previous investigations have probed 3–8 conditions, here we generated and quantified 23 unique monodisperse droplet populations for this surfactant system, demonstrating droplet stability across broad flow rate and droplet size ranges (Table 1 and S5†).

4. Investigation of common biological solutions reveals wide range of interfacial tension and viscosities

Next, we expanded our investigation of DE size to include 6 biologically relevant buffers and surfactants used in applications including bacterial growth assays, mammalian and bacterial cell lysis for NGS applications, and ddPCR (Table 3). Rheological and interfacial properties of fluorinated oils and biological buffers as typically used in droplet generation for dual layer structures and multi-surfactant systems have been largely understudied to the best of our knowledge.[1] To probe this question, we first quantified the viscosity of each buffer using a cone and plate rheometer and the interfacial tension (IFT) of buffer/oil interfaces using pendant drop tensiometry (Fig. 3 and S7,† Tables 2 and S1†).[66,67] These data reveal that: (1) these 6 different buffers span a wide range of viscosities (0.861–3.431 mPa s) and IFT values (0.543–12.41 mN m^{-1}), (2) oil surfactants heavily influence IFT, driving a nearly 100-fold decrease in IFT (PBS in oil *vs.* PBS in surfactant oil: 40 *vs.* 0.543 mN m^{-1}), (3) added salt initially lowers IFT and increases droplet deformation but high concentration can reverse this effect, and (4) outer sheath formulations, which contain both a non-ionic polysorbate surfactant and a long-chain detergent, have near-equal IFT, despite large variations in IFT in their respective inner solutions without these emulsifiers (Fig. 3C, Table 2). These results highlight the importance of oil surfactant in lowering interfacial tension and thus promoting droplet deformation. In addition, the observed nonlinear dependence of IFT on salt concentration is consistent with changes in the hydrophilic–lipophilic balance (HLB), the fraction of interface surfactant molecules in the oil *versus* aqueous phases (Fig. S6†). These positional changes lead to an initial decrease and subsequent increase in IFT as salt concentration increases and pushes the molecule out of the aqueous phase into the oil phase[68,69] (ESI† Extended Discussion Note 2).

5. DE stability depends on physical properties of inner solution

Next, we conducted size parametric sweeps across each of these 6 biologically-relevant solutions (Fig. 3A, B and S4,† Table 1). In total, we profiled thousands of droplets for each of 196 buffer and flow rate combinations (Tables S5–S7†). For each buffer condition, 14–30 flow rate combinations systematically sampled across the parameter space yielded monodisperse single core droplets, all with <5% CV in droplet inner and outer diameter (Fig. S5†), the gold standard for robust droplet generation. As seen previously (Fig. 2), droplet volume and diameter varied linearly with changing Q_1 and Q_2 and total droplet volume remained relatively constant (Fig. 3B and S4†). Consistent with prior reports for two-step formation devices, we observed only two periodic DE generation regimes, dripping–dripping and dripping–jetting formation.[1]

Table 1 Global statistics for all conditions

	PBS	PBS 1% Tween-20	PBS 1% Tween-20 replicate	Np40	Np40 replicate	PEG 10%	M9	M9 glucose	Total
Number of stable points	14	19	23	31	21	26	32	30	196
Number of instabilities imaged	0	4	1	4	4	3	3	1	20
Number of instabilities recorded	8	16	10	11	10	6	6	7	74
Number of trials	22	39	34	46	35	35	41	38	290
Number of droplets analyzed	1349	1679	2238	3157	2090	3309	3711	3399	20 932
Resultant mean outer diameter CV for stable conditions	0.014	0.021614	0.011	0.014889	0.020847	0.019	0.019321	0.018	0.017333875
Resultant mean inner diameter CV for stable conditions	0.01829	0.015135	0.015822	0.012758	0.015036	0.012793	0.013209	0.018702	0.015218125

Table 2 Interfacial and bulk fluid parameters

Surfactant system	Phase	Components	Density (kg m^{-3})	Dynamic viscosity (mPa s)	Interfacial tension with oil (mN m^{-1})
PBS	Inner	PBS	1005.58	0.931	0.543
	Middle	HFE-7500 + 2.2% ionic Krytox	1619.72	1.613	n/a
	Outer	PBS + 1% Tween-20 + 2% Pluronic-F68	1007.97	1.303	0.318
PBS + 1% Tween-20	Inner	PBS + 1% Tween-20	1006.48	0.988	0.319
	Middle	HFE-7500 + 2.2% ionic Krytox	1619.72	1.613	n/a
	Outer	PBS + 1% Tween-20 + 2% Pluronic-F68	1007.97	1.303	0.318
PBS + 0.9% NP40	Inner	PBS + 0.9% NP40 inner	1006.07	1.003	1.41
	Middle	HFE-7500 + 2.2% ionic Krytox	1619.72	1.613	n/a
	Outer	PBS + 1% Tween-20 + 2% Pluronic-F68	1007.97	1.303	0.318
M9 bacterial media	Inner	M9 salts	1013.0	0.861	12.84
	Middle	HFE-7500 + 2.2% ionic Krytox	1619.72	1.613	n/a
	Outer	M9 salts + 2% Pluronic-F68	1013.4	1.412	0.5220
M9 + 25 mM glucose	Inner	M9 salts + 25 mM glucose	1017.5	0.967	11.600
	Middle	HFE-7500 + 2.2% ionic Krytox	1619.72	1.613	n/a
	Outer	M9 salts + 25 mM glucose + 2% Pluronic-F68	1017.9	1.563	0.4580
PBS + 10% PEG 6000 mw	Inner	PBS + 10% PEG 6000 mw	1013.7	3.431	0.4613
	Middle	HFE-7500 + 2.2% ionic Krytox	1619.72	1.613	n/a
	Outer	PBS + 10% PEG 6000 mw + 2% Pluronic-F68	1014.1	6.395	0.4550

Table 3 Typical biological assays associated with each buffer

Surfactant system	Biological relevance
PBS	Base salt buffer
PBS + 1% Tween-20	Gentle cellular lysis (mammalian and bacterial)
PBS + 0.9% NP40	Cellular lysis (scATAC-Seq and other NGS)
M9 bacterial media	Bacterial growth media
M9 + 25 mM glucose	Bacterial growth media with carbon source
PBS + 10% PEG 6000 mw	Molecular crowding agent for ddPCR and other droplet molecular biology

The flow rate ranges over which each buffer yielded stable single core droplets differed dramatically (Table S5†). For example, DEs containing a high viscosity 10% PEG inner buffer were stable over a much narrower range of Q_1 flow rates than those with the M9 high-salt media containing sugars (150–220 μl h^{-1} *vs.* 150–350 μl h^{-1}, respectively) (Table S5†). Furthermore, the range of stable flow rates often differed significantly between Q_1 and Q_2: for instance, 10% PEG DEs have a very narrow range of stable flow rates in Q_1 (150–220 μl h^{-1}) but a large range of stable flow rates in Q_2 (350–1200 μl h^{-1}) (Table S5†). These differential effects on droplet stability may be explained by the interplay between viscous stresses and interfacial stresses acting on the fluid streams, as disruptions in this balance lead to instabilities, deviations from ideal flow behavior.[1,24] For single core monodisperse droplets, we define ideal flow behavior as the dripping–dripping flow regime with matching periodicity between W/O droplet generation at FF1 and W/O/W droplet formation at FF2; deviation in flow behavior, or instabilities, are caused by changing flow dynamics at the flow focusers, due to differing fluid properties with differing surfactants (Fig. S8 and S11†).

To quantify this balance of forces in the flow behavior, we then used these flow rates and the measured fluid properties to calculate capillary number Ca for each fluid condition, which specifically quantifies the strength of viscous forces relative to cohesive forces at an interface. For DE droplets, Ca_m determines the formation behavior of inner droplets and the pinch-off mechanics of the fast-flowing middle oil phase while Ca_i and Ca_o focus on the properties of the inner and outer phases respectively:[24,25]

$$Ca_i = \frac{\mu_i U_i}{\sigma_{im}} \quad (1)$$

$$Ca_m = \frac{\mu_m U_m}{\sigma_{im}} \quad (2)$$

$$Ca_o = \frac{\mu_o U_o}{\sigma_{om}} \quad (3)$$

where μ is the dynamic viscosity of the liquid, U is the characteristic velocity (here a quotient of flow rate Q_x and nozzle cross sectional area), and σ is the interfacial tension between two phases.

When visualized non-dimensionally in a plot of Ca_m *vs.* the Q_1/Q_2 ratio (Fig. 3D), different types of droplet instabilities reproducibly cluster together across conditions. Low Q_1 relative to Q_2 typically leads to oil-only coreless droplets or satellite oils, independent of Ca_m (Fig. 3D, left). At a high Q_1 relative to Q_2, instability type varies with Ca_m, with high likelihood of streaming inner phase instabilities giving way to higher likelihood of multi-core (tiny double and doublet) instabilities

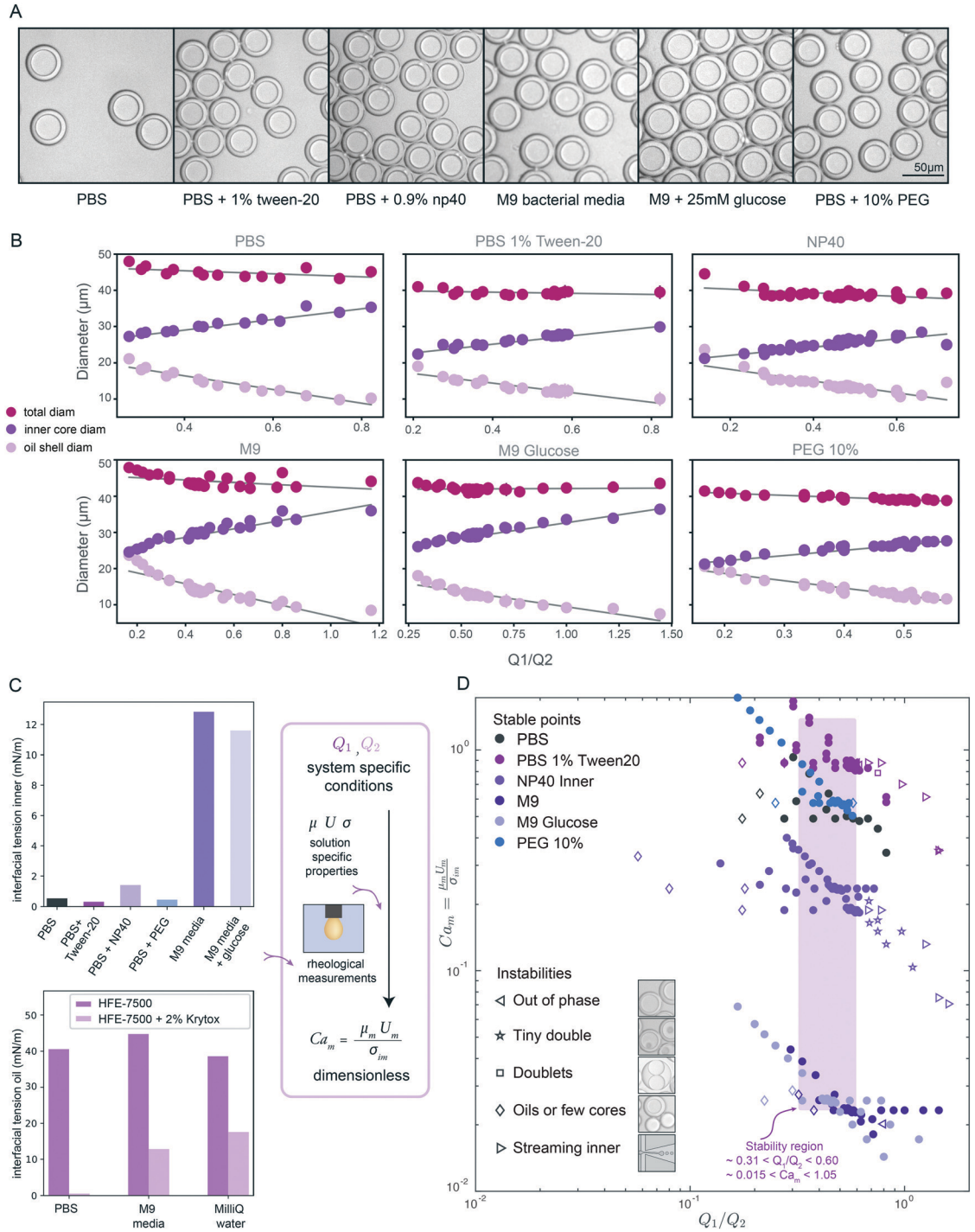

Fig. 3 DE droplet stability and morphology across varying inner core solutions & surfactants. (A) Representative bright field images of monodisperse DE droplets containing 6 different biologically relevant inner solutions. (B) Measured total (magenta markers), oil shell (lavender), and inner core (purple) diameters as a function of flow rate ratio for all conditions for each buffer. Markers indicate mean diameters (N for each condition in Table S5†) and error bars indicate standard deviation. (C) Measured interfacial tension for 6 inner aqueous solutions in the presence of HFE-7500 oil + 2.2% ionic Krytox (top), and for HFE-7500 oil with (light purple) and without (dark purple) 2.2% ionic Krytox across 3 aqueous inner solutions; measurements can be combined with flow rates to calculate dimensionless capillary numbers. (D) Capillary number Ca_m *vs.* Q_1/Q_2 flow rate ratio across all flow rate combinations and buffer conditions. Solid markers indicate conditions that yield monodisperse single core DEs; open markers indicate unstable conditions that yield droplets with mixed morphologies. Purple box indicates flow rate ratio range that produces stable monodisperse droplets across all conditions.

as Ca_m decreases (Fig. 3D, right). Droplets containing fluids with higher Ca_m transition to streaming and other instabilities at a lower Q_1/Q_2 ratio than those with lower Ca_m, while low Ca_m systems result in coreless droplets at higher Q_1/Q_2 ratios than high Ca_m systems. These droplet morphologies result from deviations from ideal flow behavior into unmatched periodicity at FF2 and the dripping–jetting regime (ESI† Extended Discussion Note 3).

Across all buffer conditions, we identify a single range of flow rate ratios that universally yields stable monodisperse single core droplets (Fig. 3D, purple box; approximately $0.31 < Q_1/Q_2 < 0.60$, $0.015 < Ca_m < 1.05$, for similar flow rates), providing an initial flow rate combination to use when trying to optimize DE generation in novel biological systems.

6. Universal size law reveals heavy dependence on mass conservation by flow rate for monodisperse droplets

A single equation capable of accurately predicting droplet size as a function of fluid properties and flow rates could significantly reduce the time, effort, and reagents required to identify optimal flow rates for a new buffer condition. Wang *et al.*[1] recently conducted an extensive computational study of formation dynamics in dual flow focuser devices, and developed a size scaling law for DE droplets formed in a one-step regime as a function of flow rates and fluid properties, building on previous size scaling laws.[63,64,70] Here, we test if this law can be applied to predict droplet sizes for single core DE droplets produced within our two-step formation device geometry. Five empirically-derived fit parameters allow the

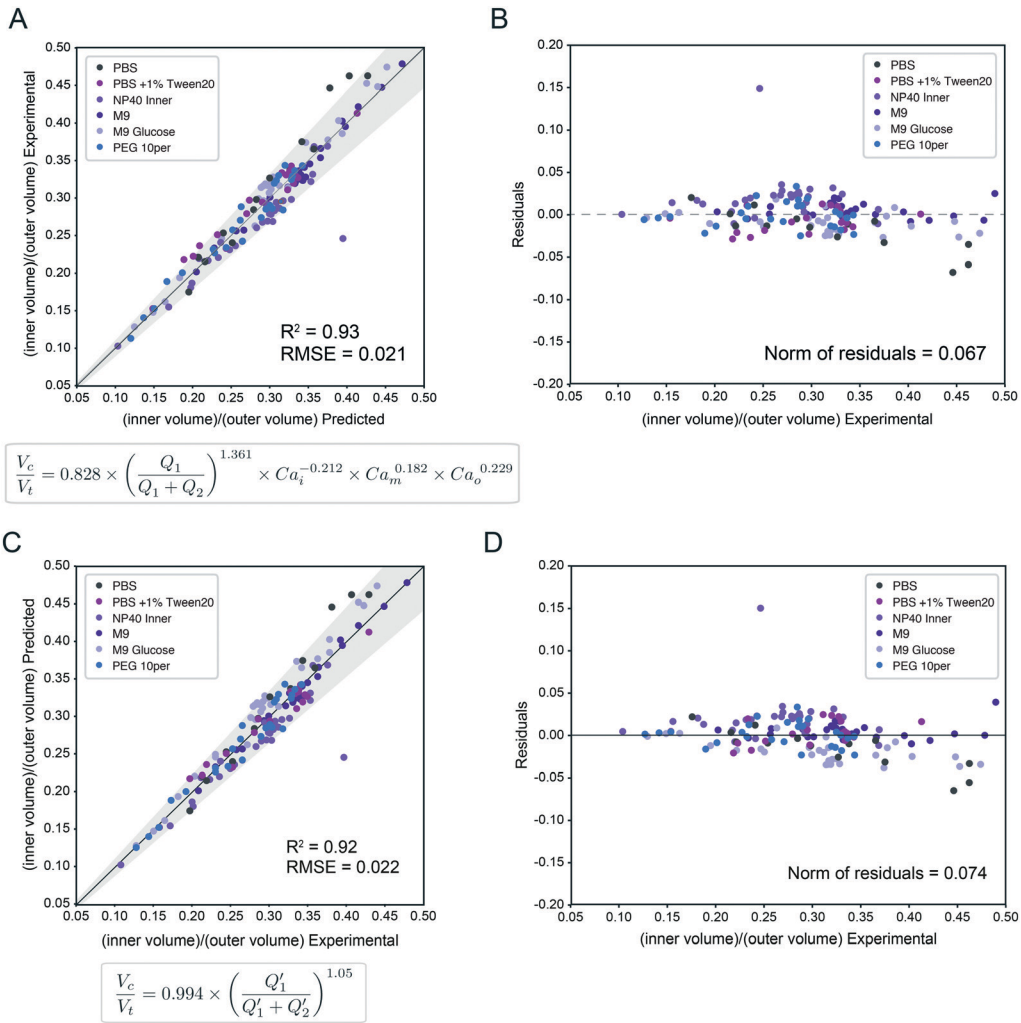

Fig. 4 Universal size scaling law capable of predicting volume ratio as a function of flow rates and capillary numbers. (Left) Predicted *vs.* experimental core volume: total volume ratio for 196 droplet conditions with buffer composition indicated by marker color. Dark line indicates 1 : 1 line; light line indicates linear regression; grey shading indicates confidence interval; universal size scaling law equation is shown below; markers indicate mean value per condition with number of droplets listed in Table S5.† (Right) Calculated residuals of experimental results from model as a function of volume. (A and B) Model A, a general form with capillary number dependence – most broadly applicable. Explains 95% of observations within a 10.7% interval. (C and D) Model B, without capillary numbers, a simplification toward ideal mass conservation that is only possible with our restrictions to ideal flow behavior. Explains 95% of observations within a 11.6% interval.

model to accurately predict the relative volume of the droplet core to the total size ($V_c : V_t$ core: total volume ratio) for 95% of the observations across all 138 conditions within an 10.7% margin (Fig. 4A, Table S8,† model A), with normally distributed residuals (Fig. 4B):

$$\frac{V_c}{V_t} = 0.828 \times \left(\frac{Q_1}{Q_1 + Q_2}\right)^{1.361} \times \mathrm{Ca_i}^{-0.212} \times \mathrm{Ca_m}^{0.182} \times \mathrm{Ca_o}^{0.229} \quad (4)$$

In this size law, the relative volume of the droplet core compared to total volume has a high dependence on relative flow rate contributions of the inner solution (Q_1) to oil (Q_2), with small exponents on $\mathrm{Ca_m}$ and $\mathrm{Ca_o}$ intimating little dependence on the outer sheath (Q_3). Because Q_3 is held constant throughout and thus measured outer droplet diameter shows only small deviations, this size law also returns information about absolute droplet size (Fig. 3B).

Our restrictions to ideal flow behavior then allow us to simplify the model to exclude capillary number dependence *via* reduced and zero exponents for $\mathrm{Ca_x}$ terms (Fig. S9B, Tables S8 and S9,† model B). A simplified model resulting from the best fit of these analyses explains 95% of observations within a margin of 11.6% (Tables S8 and S9†):

$$\frac{V_c}{V_t} = 0.994 \times \left(\frac{Q_1}{Q_1 + Q_2}\right)^{1.05} \quad (5)$$

Interestingly, we find that our model incorporating capillary number terms performed only slightly better than the simplified model that does not (R^2 = 92.5% *vs.* 93.1%, interval of explained observations = 10.7% *vs.* 11.6%, Fig. 4 and S9, Table S8†), suggesting that droplet size is determined primarily by simple mass conservation. Ideal mass conservation leads the prefactor and exponent to both be 1, and we observe the fitted parameters are very close to 1. This phenomenon is because generation of single-core double emulsions using our two-step flow regime approaches ideal behavior; our dual linear flow focuser device geometry promotes dripping–dripping and, because FF1 and FF2 are decoupled by a flow resistor, allows a user to easily match periodicity of single emulsion generation at FF1 to double emulsion encapsulation at FF2 (matched periodicity at Q_3 pinch off) by adjusting relative Q_1 and Q_2 contributions (Fig. S11, ESI† Extended Discussion Note 3). When instabilities that depart from this ideal behavior (Fig. 3D) are included, the model deviates (Fig. S10†). Thus, the simple mass

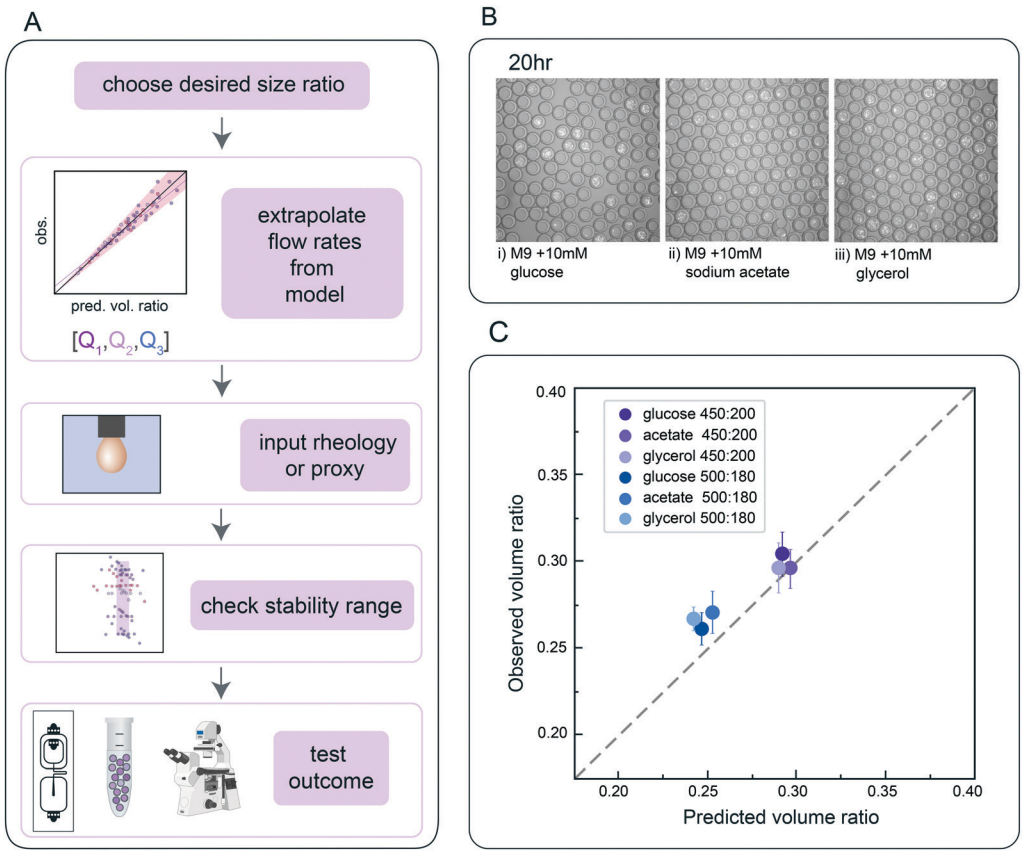

Fig. 5 Predicting flow rates required to produce droplets with a desired geometry for anaerobic *E. coli* growth assays. (A) Schematic of workflow to test accuracy of flow rate predictions from universal size scaling laws. (B) Representative microscopy images of *E. coli* growth in DEs containing M9 media plus three different carbon sources after 20 hours. (C) Measured *vs.* predicted core: total volume ratios. Markers represent mean of 10 droplets and error bars show standard deviation. Dashed line is 1 : 1 relationship.

conservation model and absolute flow rate conditions explored here, generated with our restrictions in place, apply across systems, where these assumptions are maintained. Where analyses lead to deviations from this procedure, the model can be used to provide specific predictive value (as shown in Fig. 5) if flow rates are restrained to the stable range (Fig. 3D) and minor adjustments in Q_1 & Q_2 are made to match periodicity with Q_3 to achieve monodisperse single core droplets. An alternative capillary number based model expression without a prefactor and an inner core volume model had equivalent and less optimal fits respectively (ESI† Extended Discussion 4, Fig. S9, Tables S8 and S9). The more general capillary number-based model is important for occasions when the ideal flow behavior breaks down, at instability boundaries and in schemes outside our restrictions.

These data and corresponding models are a valuable resource for flow rates that generate single core DE droplets suitable for FACS regardless of surfactant, when using this two-step device with conditions of flow regime and periodicity satisfied.

7. Size law accurately predicts size in *de novo* biological use cases

Finally, we directly validated the predictive power of this universal size scaling law *via* blind predictions of droplet stability and size for a biological assay using a previously uncharacterized inner buffer. Microfluidic encapsulation of single bacteria into droplets can enable a wide variety of applications, from high-throughput screening for media conditions that allow recovery of previously uncultured bacteria from metagenomic samples to screens for antibiotic resistance strains in a mixed community.[71–74] Such growth assays typically require M9 media supplemented with physiologically-relevant carbon sources (*e.g.* glucose, sodium acetate, or glycerol) to tune relative bacterial growth rates. To test if our universal size scaling law can help identify conditions that produce droplets of a desired size and shell thickness (mimicking the same process a user might employ), we: (1) specified 2 desired final core volume: total droplet volume ratios (0.25 and 0.30), (2) measured the dynamic viscosity (μ) and interfacial tension (σ) for M9 with either 10 mM glucose, sodium acetate, or glycerol catabolic substrates in the presence of HFE-7500 supplemented with 2.2% ionic Krytox, (3) solved for Q_1 and Q_2 flow rates that would generate droplets with the desired volume ratios using both models, which returned similar flow rates, (4) generated DE droplets encapsulating a GFP-expressing *E. coli* strain bacteria in each media with these specified flow rates, and (5) quantified actual droplet size and shell thickness (Fig. 5A).

Flow rates suggested by the models fell within the range previously found to generate stable droplets in the size characterization data (Fig. 3D). For all 3 media formulations, flow rates of [200, 450] and [180, 500] (Q_1, Q_2) yielded monodisperse single core droplets with few aberrations (Fig. 5B and C); measured volume ratios were consistent with predictions within 10.5%, 14.9% and 11.3% variation for M9 with 10 mM glucose, sodium acetate, and glycerol, respectively, for 95% of observations for the model considering only mass conservation (model C), and 8.3%, 10.0% and 10.6% for the model incorporating capillary numbers (model A). These results thereby validate the primary dependence on mass conservation seen in the systematic sweep data (Fig. 4). As expected, *E. coli* cells cultivated in double emulsions for 20 h at 37 °C grew on all three catabolic substrates in both flow conditions (Fig. 5 and S12†). The agreement between predictions and empirical measurements of DE size demonstrates, along with direct flow rate options, the utility of these tools in developing novel biological applications for single core double emulsions.

Conclusions

Double emulsion droplets are nanoliter-to-picoliter volume reactors that can be sorted by their fluorescence using commercial flow cytometers, and therefore provide a powerful tool for ultra high-throughput biochemical and cellular assays. However, production of DE droplets has long been considered technically challenging due to their complex 3-phase architecture (an inner aqueous core surrounded by an oil shell suspended within an aqueous outer buffer) and the importance of DE droplet size and shell thickness for downstream assay efficiency. Here, we performed systematic parameterization of droplet size and shell thickness over 196 different combinations of flow rates and inner buffers (>22 000 DE droplets in total) using a straightforward two-step device. Our restrictions to a dripping–dripping regime and matching Q_3 periodicity focused our investigation on single core monodisperse droplets, essential for FACS applications, and bulk and interfacial characterization of each buffer led to identification of a consistent stable flow rate ratio range. With these data, we applied and empirically validated a recent size scaling law to accurately predict DE droplet size and shell thickness as a function of flow rates and buffer properties. This dataset and model establish a valuable resource for implementation of new assays by streamlining identification of appropriate flow rates.

Further expansions of this work to additional surfactants, including reagents such as BSA and proteins that have more complex viscoelastic or skinning effects, could allow better understanding of these complex flows and further simplify novel assay development. Additionally, oil surfactants have a large effect on reaction efficiency and cell viability in droplets. Here, we held our oil formulation constant to that optimized in our prior DE FACS workflow, but effects of oil variation on droplet size and stability remain underexplored. While it seems that droplets of varying shell thickness do survive FACS, thick-shelled droplets appear anecdotally to run more slowly and cause more clogging; quantification of these trends would assist in FACS implementation. Lastly, adjustments of Q_3 for emulsions containing multiple cores may have utility in complex biological systems and would be a logical expansion of this model.

As one of the first in-depth parameterizations of DE size and stability and with an explicit focus on monodisperse single core droplets, we anticipate that this systematic dataset and size scaling model will allow users to reliably generate DE droplets with a desired size phenotype for HT biological screens *via* FACS.

Materials and methods

A. Device lithography

All designs were generated in AutoCAD (Autodesk). All designs used in the study at all stages of iteration are available on an Open Science Framework project. Devices were fabricated *via* standard soft lithography protocols as described previously.[16,31] Selective hydrophilic wettability was imparted to FF2 *via* air plasma treatment for 10 minutes with tape applied to cover outlet and outer sheath inlets as described previously.[31,75]

B. Droplet generation

DEs were generated using 3 syringe pumps (PicoPump Elite, Harvard Apparatus) for the inner, oil, and outer carrier fluids. Syringes (1–10 mL; PlastiPak plastic syringes, BD) were connected to the microfluidic device with polyethylene tubing (PE/2, Scientific Commodities). Droplet generation rates were typically 1–10 kHz. For the initial condition (Fig. 2), the inner phase for the aqueous droplet core was composed of 1% Tween-20 (Sigma) and FITC-BSA in 1x PBS (Invitrogen). For all measurements, the oil phase was composed of HFE-7500 (Sigma) and 2.2% Ionic PEG-Krytox (FSH 157, Miller-Stephenson) and the outer phase was composed of 1% Tween-20 (Sigma) and 2% Pluronic F68 (Kluplour 188, Sigma) in PBS. Typical flow rates were 400 : 230 : 6500 (O : I : C) μL h^{-1}. Droplet generation was monitored and recorded *via* a stereoscope (Amscope) and high-speed CMOS camera (ASI 174MM, ZWO). Droplets were stabilized for 4 minutes prior to a set collection time of 6 minutes. At each condition, we acquired a 500-frame video to assess stability and breakoff phenotype.

C. Study design – choice of flow rates per buffer

For each condition, we first identified a flow rate ratio that produced monodisperse droplets with a core volume : shell volume ratio close to 0.60. Next, we generated droplets at 4 flow rate combinations closely spaced around this initial condition (±5 μl h^{-1}), then varied flow rates by larger intervals to scan for the limits of the flow rate ratio regime capable of stably generating monodisperse droplets. For the Q_t sweep, we divided the expected stable range of Q_1 or Q_2 into 6 parts and inversely varied Q_1 and Q_2 to maintain a constant Q_t. In each condition, we stabilized for 4 minutes and then collected DEs for 6 minutes, allowing for assessment of a statistical population *via* microscopy. Each set of flow rate ratios contained >10 stable points and >5 unstable points across the bounds of the dynamic range recorded (Table 1).

D. Image acquisition

Prior to imaging, we loaded approximately 2 μl from the droplet pellet and 8 μl of aqueous outer solution into Countess cell counting chamber slides, forming a droplet monolayer. We then imaged droplets on a Nikon Ti Eclipse microscope at 10× magnification using both brightfield illumination and a FITC-compatible fluorescence channel. Multiple images were acquired per droplet population (>10 images per condition) in non-overlapping FOVs for FOVs containing a single layer of DE droplets. We found that accurate focus and waiting for droplets to stabilize to minimize drifting were important for accurate image analysis downstream. For each condition, we acquired a 500-frame video of droplet generation using ASICAP software just after starting droplet collection.

E. Droplet size characterization

Droplets from 10 images per flow condition were characterized in MATLAB using a custom image processing pipeline available in our Open Science Framework: **https://osf.io/pt6qu/?view_only=f1690e6efd7a4773b7e26fec5a65aada**.

F. Interfacial tension measurements: pendant drop

Interfacial tension (IFT) of each solution was measured *via* pendant drop tensiometry using drop shape analysis[66,67,76] As the oil is denser than the inner solutions, we utilized a pendant oil droplet suspended within an inner aqueous buffer solution for the analysis (Fig. S7†). Oil droplets were formed and suspended from a syringe with a 27 gauge metal capillary nozzle, within a 5 mL bulk of an inner solution. Droplet shape analysis using a custom Matlab code was conducted when the droplet was as stable as possible, as is established in the rheology literature.[66,76] At equilibrium with a stationary drop, cohesive forces (interfacial tension) and gravitational deformation are balanced. Therefore, the simplified Young–Laplace equation and the hydrostatic pressure can be equated and solved, giving interfacial tension. Final IFT measurements were the mean of calculations from 3–4 analyzed drops.

G. Viscosity measurements

Dynamic viscosity for each solution was measured using a commercial rotational cone and plate rheometer. Measurements were obtained by conducting a logarithmic flow sweep across 4 orders of magnitude of shear rate (2.86479–2864.79 Hz) with a 2° cone at 20 °C. The average viscosity in the linear regime is reported as the shear rate independent viscosity of the medium.

H. Size scaling law fitting method

For each model, a function that accepts capillary numbers, flow rate ratios, and unknown coefficients was defined in Python3. The curve_fit function in the SciPy optimization package was used to estimate best fit values for these

coefficients based on experimental data. Depending on the desired prediction, either inner-to-outer volume ratios or inner volumes as the dependent data were calculated based on known capillary numbers as the independent data. In all cases, we used an initial guess of 1 for each parameter. The curve_fit function returned optimal values for the unknown parameters and their estimated covariance.

I. *E. coli* growth – biological test case method

E. coli-GFP was routinely cultivated on Luria–Bertani (LB) agar plates supplemented with 30 μg mL^{-1} kanamycin and liquid M9 basal medium with 25 mM glucose at 37 °C. Overnight stationary phase cultures were washed twice with basal M9 medium to remove any residual carbon source. Washed cells were diluted to an optical density (OD_{600}) ~ 0.05 in the inner solution to achieve single cell loading based on a Poisson distribution. Diluted cell suspensions were supplemented with either 10 mM of glucose, acetate, or glycerol and used as inner solutions. The outer solution contained M9 medium supplemented with 2% Pluronic and 1% Tween-20 for stable droplet formation. After generation of double emulsions, the outer solution was replaced with M9 medium containing only 2% Pluronic to ensure *E. coli*-GFP grew on the packaged substrate, rather than catabolizing Tween-20 surfactant. *E. coli*-GFP double emulsions were incubated statically at 37 °C overnight. Microscopy samples were imaged at 0 and 20 h timepoints to measure droplet sizes and *E. coli*-GFP fluorescence.

Conflicts of interest

Methods and techniques outlined in this work are disclosed in a U.S. patent filing, U.S. PTO Application No. 62/693800, filed by co-authors K. K. B. and P. M. F. and Sandy Klemm.

Acknowledgements

The authors thank Rochelle Radzyminski and Margarita Khariton for their help with image processing and discussion during the formulation of this study. We are grateful to all members of the Dropception team as well as Fordyce, Fuller and Kusumaatmaja laboratories for their advice and helpful feedback on the manuscript. S. G. K. C. acknowledges funding as a ChEM-H CBI fellow and a Stanford Graduate SGF fellow. K. K. B. acknowledges funding as ChEM-H CBI fellow, an NSF GFRP fellow, and a Siebel Scholar. A. L. M. acknowledges funding as a Simons Foundation Postdoctoral Fellow in Marine Microbial Ecology (award #600755). P. M. F. is a Chan Zuckerberg Biohub Investigator and this work was supported by NIH DP2-GM123641 awarded to P. M. F.

References

1 N. Wang, C. Semprebon, H. Liu, C. Zhang and H. Kusumaatmaja, Modelling Double Emulsion Formation in Planar Flow-Focusing Microchannels, *J. Fluid Mech.*, 2020, **895**, A22, DOI: **10.1017/jfm.2020.299**.

2 J. Clausell-Tormos, D. Lieber, J.-C. Baret, A. El-Harrak, O. J. Miller, L. Frenz, J. Blouwolff, K. J. Humphry, S. Köster, H. Duan, C. Holtze, D. A. Weitz, A. D. Griffiths and C. A. Merten, Droplet-Based Microfluidic Platforms for the Encapsulation and Screening of Mammalian Cells and Multicellular Organisms, *Chem. Biol.*, 2008, **15**(5), 427–437, DOI: **10.1016/j.chembiol.2008.04.004**.

3 J. Q. Boedicker, L. Li, T. R. Kline and R. F. Ismagilov, Detecting Bacteria and Determining Their Susceptibility to Antibiotics by Stochastic Confinement in Nanoliter Droplets Using Plug-Based Microfluidics, *Lab Chip*, 2008, **8**(8), 1265, DOI: **10.1039/b804911d**.

4 D. J. Sukovich, S. T. Lance and A. R. Abate, Sequence Specific Sorting of DNA Molecules with FACS Using 3dPCR, *Sci. Rep.*, 2017, **7**(1), 39385, DOI: **10.1038/srep39385**.

5 E. Mastrobattista, V. Taly, E. Chanudet, P. Treacy, B. T. Kelly and A. D. Griffiths, High-Throughput Screening of Enzyme Libraries: In Vitro Evolution of a β-Galactosidase by Fluorescence-Activated Sorting of Double Emulsions, *Chem. Biol.*, 2005, **12**(12), 1291–1300, DOI: **10.1016/j.chembiol.2005.09.016**.

6 P. Shahi, S. C. Kim, J. R. Haliburton, Z. J. Gartner and A. R. Abate, Abseq: Ultrahigh-Throughput Single Cell Protein Profiling with Droplet Microfluidic Barcoding, *Sci. Rep.*, 2017, **7**(1), 44447, DOI: **10.1038/srep44447**.

7 J. J. Agresti, E. Antipov, A. R. Abate, K. Ahn, A. C. Rowat, J.-C. Baret, M. Marquez, A. M. Klibanov, A. D. Griffiths and D. A. Weitz, Ultrahigh-Throughput Screening in Drop-Based Microfluidics for Directed Evolution, *Proc. Natl. Acad. Sci. U. S. A.*, 2010, **107**(9), 4004–4009, DOI: **10.1073/pnas.0910781107**.

8 A. Aharoni, G. Amitai, K. Bernath, S. Magdassi and D. S. Tawfik, High-Throughput Screening of Enzyme Libraries: Thiolactonases Evolved by Fluorescence-Activated Sorting of Single Cells in Emulsion Compartments, *Chem. Biol.*, 2005, **12**(12), 1281–1289, DOI: **10.1016/j.chembiol.2005.09.012**.

9 L. Granieri, J.-C. Baret, A. D. Griffiths and C. A. Merten, High-Throughput Screening of Enzymes by Retroviral Display Using Droplet-Based Microfluidics, *Chem. Biol.*, 2010, **17**(3), 229–235, DOI: **10.1016/j.chembiol.2010.02.011**.

10 S. C. Kim, I. C. Clark, P. Shahi and A. R. Abate, Single-Cell RT-PCR in Microfluidic Droplets with Integrated Chemical Lysis, *Anal. Chem.*, 2018, **90**(2), 1273–1279, DOI: **10.1021/acs.analchem.7b04050**.

11 C. A. Lareau, F. M. Duarte, J. G. Chew, V. K. Kartha, Z. D. Burkett, A. S. Kohlway, D. Pokholok, M. J. Aryee, F. J. Steemers, R. Lebofsky and J. D. Buenrostro, Droplet-Based Combinatorial Indexing for Massive-Scale Single-Cell Chromatin Accessibility, *Nat. Biotechnol.*, 2019, **37**(8), 916–924, DOI: **10.1038/s41587-019-0147-6**.

12 E. Z. Macosko, A. Basu, R. Satija, J. Nemesh, K. Shekhar, M. Goldman, I. Tirosh, A. R. Bialas, N. Kamitaki, E. M. Martersteck, J. J. Trombetta, D. A. Weitz, J. R. Sanes, A. K.

Shalek, A. Regev and S. A. McCarroll, Highly Parallel Genome-Wide Expression Profiling of Individual Cells Using Nanoliter Droplets, *Cell*, 2015, **161**(5), 1202–1214, DOI: **10.1016/j.cell.2015.05.002**.

13 D. J. Eastburn, A. Sciambi and A. R. Abate, Ultrahigh-Throughput Mammalian Single-Cell Reverse-Transcriptase Polymerase Chain Reaction in Microfluidic Drops, *Anal. Chem.*, 2013, **85**(16), 8016–8021, DOI: **10.1021/ac402057q**.

14 L. Shang, Y. Cheng and Y. Zhao, Emerging Droplet Microfluidics, *Chem. Rev.*, 2017, **117**(12), 7964–8040, DOI: **10.1021/acs.chemrev.6b00848**.

15 S. Ma, J. M. Sherwood, W. T. S. Huck and S. Balabani, The Microenvironment of Double Emulsions in Rectangular Microchannels, *Lab Chip*, 2015, **15**(10), 2327–2334, DOI: **10.1039/C5LC00346F**.

16 K. K. Brower, C. Carswell-Crumpton, S. Klemm, B. Cruz, G. Kim, S. G. K. Calhoun, L. Nichols and P. M. Fordyce, Double Emulsion Flow Cytometry with High-Throughput Single Droplet Isolation and Nucleic Acid Recovery, *Lab Chip*, 2020, **20**(12), 2062–2074, DOI: **10.1039/D0LC00261E**.

17 G. Vladisavljević, R. Al Nuumani and S. Nabavi, Microfluidic Production of Multiple Emulsions, *Micromachines*, 2017, **8**(3), 75, DOI: **10.3390/mi8030075**.

18 J.-C. Chang, Z. Swank, O. Keiser, S. J. Maerkl and E. Amstad, Microfluidic Device for Real-Time Formulation of Reagents and Their Subsequent Encapsulation into Double Emulsions, *Sci. Rep.*, 2018, **8**(1), 8143, DOI: **10.1038/s41598-018-26542-x**.

19 A. Gross, J. Schoendube, S. Zimmermann, M. Steeb, R. Zengerle and P. Koltay, Technologies for Single-Cell Isolation, *Int. J. Mol. Sci.*, 2015, **16**(8), 16897–16919, DOI: **10.3390/ijms160816897**.

20 T. Stuart and R. Satija, Integrative Single-Cell Analysis, *Nat. Rev. Genet.*, 2019, **20**(5), 257–272, DOI: **10.1038/s41576-019-0093-7**.

21 J. Yan, W.-A. Bauer, M. Fischlechner, F. Hollfelder, C. Kaminski and W. Huck, Monodisperse Water-in-Oil-in-Water (W/O/W) Double Emulsion Droplets as Uniform Compartments for High-Throughput Analysis via Flow Cytometry, *Micromachines*, 2013, **4**(4), 402–413, DOI: **10.3390/mi4040402**.

22 A. Zinchenko, S. R. A. Devenish, B. Kintses, P.-Y. Colin, M. Fischlechner and F. Hollfelder, One in a Million: Flow Cytometric Sorting of Single Cell-Lysate Assays in Monodisperse Picolitre Double Emulsion Droplets for Directed Evolution, *Anal. Chem.*, 2014, **86**(5), 2526–2533, DOI: **10.1021/ac403585p**.

23 S. B. Choi, J. Y. Park, J. Y. Moon and J. S. Lee, Effect of Interactions between Multiple Interfaces on the Rheological Characteristics of Double Emulsions, *Phys. Rev. E*, 2018, **97**(6), 062603, DOI: **10.1103/PhysRevE.97.062603**.

24 P. Guillot, A. Colin, A. S. Utada and A. Ajdari, Stability of a Jet in Confined Pressure-Driven Biphasic Flows at Low Reynolds Numbers, *Phys. Rev. Lett.*, 2007, **99**(10), 104502, DOI: **10.1103/PhysRevLett.99.104502**.

25 N. M. Kovalchuk, M. Sagisaka, K. Steponavicius, D. Vigolo and M. J. H. Simmons, Drop Formation in Microfluidic Cross-Junction: Jetting to Dripping to Jetting Transition, *Microfluid. Nanofluid.*, 2019, **23**(8), 103, DOI: **10.1007/s10404-019-2269-z**.

26 L. D. Zarzar, V. Sresht, E. M. Sletten, J. A. Kalow, D. Blankschtein and T. M. Swager, Dynamically Reconfigurable Complex Emulsions via Tunable Interfacial Tensions, *Nature*, 2015, **518**(7540), 520–524, DOI: **10.1038/nature14168**.

27 A. R. Abate, J. Thiele and D. A. Weitz, One-Step Formation of Multiple Emulsions in Microfluidics, *Lab Chip*, 2011, **11**(2), 253–258, DOI: **10.1039/C0LC00236D**.

28 M.-J. Zhang, P. Zhang, L.-D. Qiu, T. Chen, W. Wang and L.-Y. Chu, Controllable Microfluidic Fabrication of Microstructured Functional Materials, *Biomicrofluidics*, 2020, **14**(6), 061501, DOI: **10.1063/5.0027907**.

29 T. Y. Lee, T. M. Choi, T. S. Shim, R. A. M. Frijns and S.-H. Kim, Microfluidic Production of Multiple Emulsions and Functional Microcapsules, *Lab Chip*, 2016, **16**(18), 3415–3440, DOI: **10.1039/C6LC00809G**.

30 Y. Zhang, Y.-P. Ho, Y.-L. Chiu, H. F. Chan, B. Chlebina, T. Schuhmann, L. You and K. W. Leong, A Programmable Microenvironment for Cellular Studies via Microfluidics-Generated Double Emulsions, *Biomaterials*, 2013, **34**(19), 4564–4572, DOI: **10.1016/j.biomaterials.2013.03.002**.

31 K. K. Brower, M. Khariton, P. H. Suzuki, C. Still, G. Kim, S. G. K. Calhoun, L. S. Qi, B. Wang and P. M. Fordyce, Double Emulsion Picoreactors for High-Throughput Single-Cell Encapsulation and Phenotyping via FACS, *Anal. Chem.*, 2020, **92**(19), 13262–13270, DOI: **10.1021/acs.analchem.0c02499**.

32 D. J. Collins, A. Neild, A. deMello, A.-Q. Liu and Y. Ai, The Poisson Distribution and beyond: Methods for Microfluidic Droplet Production and Single Cell Encapsulation, *Lab Chip*, 2015, **15**(17), 3439–3459, DOI: **10.1039/C5LC00614G**.

33 S. Ma, W. T. S. Huck and S. Balabani, Deformation of Double Emulsions under Conditions of Flow Cytometry Hydrodynamic Focusing, *Lab Chip*, 2015, **15**(22), 4291–4301, DOI: **10.1039/C5LC00693G**.

34 A. Z. Zinchenko and R. H. Davis, Extensional and Shear Flows, and General Rheology of Concentrated Emulsions of Deformable Drops, *J. Fluid Mech.*, 2015, **779**, 197–244, DOI: **10.1017/jfm.2015.411**.

35 A. Cossarizza, H. Chang, A. Radbruch, A. Acs, D. Adam, S. Adam-Klages, W. W. Agace, N. Aghaeepour, M. Akdis, M. Allez, L. N. Almeida, G. Alvisi, G. Anderson, I. Andrä, F. Annunziato, A. Anselmo, P. Bacher, C. T. Baldari, S. Bari, V. Barnaba, J. Barros-Martins, L. Battistini, W. Bauer, S. Baumgart, N. Baumgarth, D. Baumjohann, B. Baying, M. Bebawy, B. Becher, W. Beisker, V. Benes, R. Beyaert, A. Blanco, D. A. Boardman, C. Bogdan, J. G. Borger, G. Borsellino, P. E. Boulais, J. A. Bradford, D. Brenner, R. R. Brinkman, A. E. S. Brooks, D. H. Busch, M. Büscher, T. P. Bushnell, F. Calzetti, G. Cameron, I. Cammarata, X. Cao, S. L. Cardell, S. Casola, M. A. Cassatella, A. Cavani, A. Celada, L. Chatenoud, P. K. Chattopadhyay, S. Chow, E.

Christakou, L. Čičin-Šain, M. Clerici, F. S. Colombo, L. Cook, A. Cooke, A. M. Cooper, A. J. Corbett, A. Cosma, L. Cosmi, P. G. Coulie, A. Cumano, L. Cvetkovic, V. D. Dang, C. Dang-Heine, M. S. Davey, D. Davies, S. De Biasi, G. Del Zotto, G. V. Dela Cruz, M. Delacher, S. Della Bella, P. Dellabona, G. Deniz, M. Dessing, J. P. Di Santo, A. Diefenbach, F. Dieli, A. Dolf, T. Dörner, R. J. Dress, D. Dudziak, M. Dustin, C. Dutertre, F. Ebner, S. B. G. Eckle, M. Edinger, P. Eede, G. R. A. Ehrhardt, M. Eich, P. Engel, B. Engelhardt, A. Erdei, C. Esser, B. Everts, M. Evrard, C. S. Falk, T. A. Fehniger, M. Felipo-Benavent, H. Ferry, M. Feuerer, A. Filby, K. Filkor, S. Fillatreau, M. Follo, I. Förster, J. Foster, G. A. Foulds, B. Frehse, P. S. Frenette, S. Frischbutter, W. Fritzsche, D. W. Galbraith, A. Gangaev, N. Garbi, B. Gaudilliere, R. T. Gazzinelli, J. Geginat, W. Gerner, N. A. Gherardin, K. Ghoreschi, L. Gibellini, F. Ginhoux, K. Goda, D. I. Godfrey, C. Goettlinger, J. M. González-Navajas, C. S. Goodyear, A. Gori, J. L. Grogan, D. Grummitt, A. Grützkau, C. Haftmann, J. Hahn, H. Hammad, G. Hämmerling, L. Hansmann, G. Hansson, C. M. Harpur, S. Hartmann, A. Hauser, A. E. Hauser, D. L. Haviland, D. Hedley, D. C. Hernández, G. Herrera, M. Herrmann, C. Hess, T. Höfer, P. Hoffmann, K. Hogquist, T. Holland, T. Höllt, R. Holmdahl, P. Hombrink, J. P. Houston, B. F. Hoyer, B. Huang, F. Huang, J. E. Huber, J. Huehn, M. Hundemer, C. A. Hunter, W. Y. K. Hwang, A. Iannone, F. Ingelfinger, S. M. Ivison, H. Jäck, P. K. Jani, B. Jávega, S. Jonjic, T. Kaiser, T. Kalina, T. Kamradt, S. H. E. Kaufmann, B. Keller, S. L. C. Ketelaars, A. Khalilnezhad, S. Khan, J. Kisielow, P. Klenerman, J. Knopf, H. Koay, K. Kobow, J. K. Kolls, W. T. Kong, M. Kopf, T. Korn, K. Kriegsmann, H. Kristyanto, T. Kroneis, A. Krueger, J. Kühne, C. Kukat, D. Kunkel, H. Kunze-Schumacher, T. Kurosaki, C. Kurts, P. Kvistborg, I. Kwok, J. Landry, O. Lantz, P. Lanuti, F. LaRosa, A. Lehuen, S. LeibundGut-Landmann, M. D. Leipold, L. Y. T. Leung, M. K. Levings, A. C. Lino, F. Liotta, V. Litwin, Y. Liu, H. Ljunggren, M. Lohoff, G. Lombardi, L. Lopez, M. López-Botet, A. E. Lovett-Racke, E. Lubberts, H. Luche, B. Ludewig, E. Lugli, S. Lunemann, H. T. Maecker, L. Maggi, O. Maguire, F. Mair, K. H. Mair, A. Mantovani, R. A. Manz, A. J. Marshall, A. Martínez-Romero, G. Martrus, I. Marventano, W. Maslinski, G. Matarese, A. V. Mattioli, C. Maueröder, A. Mazzoni, J. McCluskey, M. McGrath, H. M. McGuire, I. B. McInnes, H. E. Mei, F. Melchers, S. Melzer, D. Mielenz, S. D. Miller, K. H. G. Mills, H. Minderman, J. Mjösberg, J. Moore, B. Moran, L. Moretta, T. R. Mosmann, S. Müller, G. Multhoff, L. E. Muñoz, C. Münz, T. Nakayama, M. Nasi, K. Neumann, L. G. Ng, A. Niedobitek, S. Nourshargh, G. Núñez, J. O'Connor, A. Ochel, A. Oja, D. Ordonez, A. Orfao, E. Orlowski-Oliver, W. Ouyang, A. Oxenius, R. Palankar, I. Panse, K. Pattanapanyasat, M. Paulsen, D. Pavlinic, L. Penter, P. Peterson, C. Peth, J. Petriz, F. Piancone, W. F. Pickl, S. Piconese, M. Pinti, A. G. Pockley, M. J. Podolska, Z. Poon, K. Pracht, I. Prinz, C. E. M. Pucillo, S. A. Quataert, L. Quatrini, K. M. Quinn, H. Radbruch, T. R. D. J. Radstake, S. Rahmig, H. Rahn, B. Rajwa, G. Ravichandran, Y. Raz, J. A. Rebhahn, D. Recktenwald, D. Reimer, C. Reis e Sousa, E. B. M. Remmerswaal, L. Richter, L. G. Rico, A. Riddell, A. M. Rieger, J. P. Robinson, C. Romagnani, A. Rubartelli, J. Ruland, A. Saalmüller, Y. Saeys, T. Saito, S. Sakaguchi, F. Sala-de-Oyanguren, Y. Samstag, S. Sanderson, I. Sandrock, A. Santoni, R. B. Sanz, M. Saresella, C. Sautes-Fridman, B. Sawitzki, L. Schadt, A. Scheffold, H. U. Scherer, M. Schiemann, F. A. Schildberg, E. Schimisky, A. Schlitzer, J. Schlosser, S. Schmid, S. Schmitt, K. Schober, D. Schraivogel, W. Schuh, T. Schüler, R. Schulte, A. R. Schulz, S. R. Schulz, C. Scottá, D. Scott-Algara, D. P. Sester, T. V. Shankey, B. Silva-Santos, A. K. Simon, K. M. Sitnik, S. Sozzani, D. E. Speiser, J. Spidlen, A. Stahlberg, A. M. Stall, N. Stanley, R. Stark, C. Stehle, T. Steinmetz, H. Stockinger, Y. Takahama, K. Takeda, L. Tan, A. Tárnok, G. Tiegs, G. Toldi, J. Tornack, E. Traggiai, M. Trebak, T. I. M. Tree, J. Trotter, J. Trowsdale, M. Tsoumakidou, H. Ulrich, S. Urbanczyk, W. Veen, M. Broek, E. Pol, S. Van Gassen, G. Van Isterdael, R. A. W. Lier, M. Veldhoen, S. Vento-Asturias, P. Vieira, D. Voehringer, H. Volk, A. Borstel, K. Volkmann, A. Waisman, R. V. Walker, P. K. Wallace, S. A. Wang, X. M. Wang, M. D. Ward, K. A. Ward-Hartstonge, K. Warnatz, G. Warnes, S. Warth, C. Waskow, J. V. Watson, C. Watzl, L. Wegener, T. Weisenburger, A. Wiedemann, J. Wienands, A. Wilharm, R. J. Wilkinson, G. Willimsky, J. B. Wing, R. Winkelmann, T. H. Winkler, O. F. Wirz, A. Wong, P. Wurst, J. H. M. Yang, J. Yang, M. Yazdanbakhsh, L. Yu, A. Yue, H. Zhang, Y. Zhao, S. M. Ziegler, C. Zielinski, J. Zimmermann and A. Zychlinsky, Guidelines for the Use of Flow Cytometry and Cell Sorting in Immunological Studies (Second Edition), *Eur. J. Immunol.*, 2019, **49**(10), 1457–1973, DOI: **10.1002/eji.201970107**.

36 J. E. López, J. Sharma, J. Avila, T. S. Wood, J. E. VanDyke, B. McLaughlin, C. K. Abbey, A. Wong, B.-E. Myagmar, P. M. Swigart, P. C. Simpson and N. Chiamvimonvat, Novel Large-Particle FACS Purification of Adult Ventricular Myocytes Reveals Accumulation of Myosin and Actin Disproportionate to Cell Size and Proteome in Normal Post-Weaning Development, *J. Mol. Cell. Cardiol.*, 2017, **111**, 114–122, DOI: **10.1016/j.yjmcc.2017.07.012**.

37 S. Kim and S. Dabiri, Transient Dynamics of Eccentric Double Emulsion Droplets in a Simple Shear Flow, *Phys. Rev. Fluids*, 2017, **2**(10), 104305, DOI: **10.1103/PhysRevFluids.2.104305**.

38 A. S. Opalski, K. Makuch, L. Derzsi and P. Garstecki, Split or Slip – Passive Generation of Monodisperse Double Emulsions with Cores of Varying Viscosity in Microfluidic Tandem Step Emulsification System, *RSC Adv.*, 2020, **10**(39), 23058–23065, DOI: **10.1039/D0RA03007D**.

39 C. Holtze, A. C. Rowat, J. J. Agresti, J. B. Hutchison, F. E. Angilè, C. H. J. Schmitz, S. Köster, H. Duan, K. J. Humphry, R. A. Scanga, J. S. Johnson, D. Pisignano and D. A. Weitz, Biocompatible Surfactants for Water-in-Fluorocarbon Emulsions, *Lab Chip*, 2008, **8**(10), 1632, DOI: **10.1039/b806706f**.

40 S.-H. Kim, J. W. Kim, J.-C. Cho and D. A. Weitz, Double-Emulsion Drops with Ultra-Thin Shells for Capsule

Templates, *Lab Chip*, 2011, **11**(18), 3162–3166, DOI: **10.1039/C1LC20434C**.

41 A. S. Utada, E. Lorenceau, D. R. Link, P. D. Kaplan, H. A. Stone and D. A. Weitz, Monodisperse Double Emulsions Generated from a Microcapillary Device, *Science*, 2005, **308**(5721), 537–541, DOI: **10.1126/science.1109164**.

42 G. M. Whitesides, The Origins and the Future of Microfluidics, *Nature*, 2006, **442**(7101), 368–373, DOI: **10.1038/nature05058**.

43 B. F. B. Silva, C. Rodríguez-Abreu and N. Vilanova, Recent Advances in Multiple Emulsions and Their Application as Templates, *Curr. Opin. Colloid Interface Sci.*, 2016, **25**, 98–108, DOI: **10.1016/j.cocis.2016.07.006**.

44 J. Wang, S. Hahn, E. Amstad and N. Vogel, Tailored Double Emulsions Made Simple, *Adv. Mater.*, 2022, **34**(5), 2107338, DOI: **10.1002/adma.202107338**.

45 D. J. Sukovich, S. C. Kim, N. Ahmed and A. R. Abate, Bulk Double Emulsification for Flow Cytometric Analysis of Microfluidic Droplets, *Analyst*, 2017, **142**(24), 4618–4622, DOI: **10.1039/C7AN01695F**.

46 S. A. Nabavi, G. T. Vladisavljević and V. Manović, Mechanisms and Control of Single-Step Microfluidic Generation of Multi-Core Double Emulsion Droplets, *Chem. Eng. J.*, 2017, **322**, 140–148, DOI: **10.1016/j.cej.2017.04.008**.

47 M. Kakran and M. N. Antipina, Emulsion-Based Techniques for Encapsulation in Biomedicine, Food and Personal Care, *Curr. Opin. Pharmacol.*, 2014, **18**, 47–55, DOI: **10.1016/j.coph.2014.09.003**.

48 T. Nisisako and T. Hatsuzawa, Microfluidic Fabrication of Oil-Filled Polymeric Microcapsules with Independently Controllable Size and Shell Thickness via Janus to Core–Shell Evolution of Biphasic Droplets, *Sens. Actuators, B*, 2016, **223**, 209–216, DOI: **10.1016/j.snb.2015.09.085**.

49 D. Lee and D. A. Weitz, Double Emulsion-Templated Nanoparticle Colloidosomes with Selective Permeability, *Adv. Mater.*, 2008, **20**(18), 3498–3503, DOI: **10.1002/adma.200800918**.

50 S.-H. Kim, J. W. Kim, D.-H. Kim, S.-H. Han and D. A. Weitz, Enhanced-Throughput Production of Polymersomes Using a Parallelized Capillary Microfluidic Device, *Microfluid. Nanofluid.*, 2013, **14**(3–4), 509–514, DOI: **10.1007/s10404-012-1069-5**.

51 H.-J. Oh, S.-H. Kim, J.-Y. Baek, G.-H. Seong and S.-H. Lee, Hydrodynamic Micro-Encapsulation of Aqueous Fluids and Cells via 'on the Fly' Photopolymerization, *J. Micromech. Microeng.*, 2006, **16**(2), 285–291, DOI: **10.1088/0960-1317/16/2/013**.

52 M. Seo, C. Paquet, Z. Nie, S. Xu and E. Kumacheva, Microfluidic Consecutive Flow-Focusing Droplet Generators, *Soft Matter*, 2007, **3**(8), 986, DOI: **10.1039/b700687j**.

53 P. Zhu and L. Wang, Passive and Active Droplet Generation with Microfluidics: A Review, *Lab Chip*, 2017, **17**(1), 34–75, DOI: **10.1039/C6LC01018K**.

54 S. A. Nabavi, G. T. Vladisavljević, M. V. Bandulasena, O. Arjmandi-Tash and V. Manović, Prediction and Control of Drop Formation Modes in Microfluidic Generation of Double Emulsions by Single-Step Emulsification, *J. Colloid Interface Sci.*, 2017, **505**, 315–324, DOI: **10.1016/j.jcis.2017.05.115**.

55 N. Pannacci, H. Bruus, D. Bartolo, I. Etchart, T. Lockhart, Y. Hennequin, H. Willaime and P. Tabeling, Equilibrium and Nonequilibrium States in Microfluidic Double Emulsions, *Phys. Rev. Lett.*, 2008, **101**(16), 164502, DOI: **10.1103/PhysRevLett.101.164502**.

56 A. R. Abate and D. A. Weitz, High-Order Multiple Emulsions Formed in Poly(Dimethylsiloxane) Microfluidics, *Small*, 2009, **5**(18), 2030–2032, DOI: **10.1002/smll.200900569**.

57 T. Nisisako, S. Okushima and T. Torii, Controlled Formulation of Monodisperse Double Emulsions in a Multiple-Phase Microfluidic System, *Soft Matter*, 2005, **1**(1), 23, DOI: **10.1039/b501972a**.

58 T. Nisisako, T. Ando and T. Hatsuzawa, Capillary-Assisted Fabrication of Biconcave Polymeric Microlenses from Microfluidic Ternary Emulsion Droplets, *Small*, 2014, **10**, 5116–5125, DOI: **10.1002/smll.201401269**.

59 S. Okushima, T. Nisisako, T. Torii and T. Higuchi, Controlled Production of Monodisperse Double Emulsions by Two-Step Droplet Breakup in Microfluidic Devices, *Langmuir*, 2004, **20**(23), 9905–9908, DOI: **10.1021/la0480336**.

60 M. Azarmanesh, M. Farhadi and P. Azizian, Double Emulsion Formation through Hierarchical Flow-Focusing Microchannel, *Phys. Fluids*, 2016, **28**(3), 032005, DOI: **10.1063/1.4944058**.

61 Y. Chen, L. Wu and L. Zhang, Dynamic Behaviors of Double Emulsion Formation in a Flow-Focusing Device, *Int. J. Heat Mass Transfer*, 2015, **82**, 42–50, DOI: **10.1016/j.ijheatmasstransfer.2014.11.027**.

62 S. A. Nabavi, G. T. Vladisavljević, S. Gu and E. E. Ekanem, Double Emulsion Production in Glass Capillary Microfluidic Device: Parametric Investigation of Droplet Generation Behaviour, *Chem. Eng. Sci.*, 2015, **130**, 183–196, DOI: **10.1016/j.ces.2015.03.004**.

63 Y. Fu, S. Zhao, L. Bai, Y. Jin and Y. Cheng, Numerical Study of Double Emulsion Formation in Microchannels by a Ternary Lattice Boltzmann Method, *Chem. Eng. Sci.*, 2016, **146**, 126–134, DOI: **10.1016/j.ces.2016.02.036**.

64 Z. Chang, C. A. Serra, M. Bouquey, L. Prat and G. Hadziioannou, Co-Axial Capillaries Microfluidic Device for Synthesizing Size- and Morphology-Controlled Polymer Core-Polymer Shell Particles, *Lab Chip*, 2009, **9**(20), 3007, DOI: **10.1039/b913703c**.

65 M. Li, M. van Zee, K. Goda and D. Di Carlo, Size-Based Sorting of Hydrogel Droplets Using Inertial Microfluidics, *Lab Chip*, 2018, **18**(17), 2575–2582, DOI: **10.1039/C8LC00568K**.

66 J. D. Berry, M. J. Neeson, R. R. Dagastine, D. Y. C. Chan and R. F. Tabor, Measurement of Surface and Interfacial Tension Using Pendant Drop Tensiometry, *J. Colloid Interface Sci.*, 2015, **454**, 226–237, DOI: **10.1016/j.jcis.2015.05.012**.

67 V. Chandran Suja, M. Rodríguez-Hakim, J. Tajuelo and G. G. Fuller, Single Bubble and Drop Techniques for

Characterizing Foams and Emulsions, *Adv. Colloid Interface Sci.*, 2020, **286**, 102295, DOI: **10.1016/j.cis.2020.102295**.

68 R. Aveyard, B. P. Binks, T. A. Lawless and J. Mead, Interfacial Tension Minima in Oil + Water + Surfactant Systems. Effects of Salt and Temperature in Systems Containing Non-Ionic Surfactants, *J. Chem. Soc., Faraday Trans. 1*, 1985, **81**(9), 2155, DOI: **10.1039/f19858102155**.

69 R. Granet, R. D. Khadirian and S. Piekarski, Interfacial Tension and Surfactant Distribution in Water—Oil—NaCl Systems Containing Double-Tailed Sulfonates, *Colloids Surf.*, 1990, **49**, 199–209, DOI: **10.1016/0166-6622(90)80102-A**.

70 H. Liu and Y. Zhang, Droplet Formation in Microfluidic Cross-Junctions, *Phys. Fluids*, 2011, **23**(8), 082101, DOI: **10.1063/1.3615643**.

71 J. Y. Tan, S. Wang, G. J. Dick, V. B. Young, D. H. Sherman, M. A. Burns and X. N. Lin, Co-Cultivation of Microbial Sub-Communities in Microfluidic Droplets Facilitates High-Resolution Genomic Dissection of Microbial 'Dark Matter.', *Integr. Biol.*, 2020, **12**(11), 263–274, DOI: **10.1093/intbio/zyaa021**.

72 J. Park, A. Kerner, M. A. Burns and X. N. Lin, Microdroplet-Enabled Highly Parallel Co-Cultivation of Microbial Communities, *PLoS One*, 2011, **6**(2), e17019, DOI: **10.1371/journal.pone.0017019**.

73 H. Bachmann, M. Fischlechner, I. Rabbers, N. Barfa, F. Branco dos Santos, D. Molenaar and B. Teusink, Availability of Public Goods Shapes the Evolution of Competing Metabolic Strategies, *Proc. Natl. Acad. Sci. U. S. A.*, 2013, **110**(35), 14302–14307, DOI: **10.1073/pnas.1308523110**.

74 J. A. Hernandez-Valdes, M. aan de Stegge, J. Hermans, J. Teunis, R. J. van Tatenhove-Pel, B. Teusink, H. Bachmann and O. P. Kuipers, Enhancement of Amino Acid Production and Secretion by Lactococcus Lactis Using a Droplet-Based Biosensing and Selection System, *Metab. Eng. Commun.*, 2020, **11**, e00133, DOI: **10.1016/j.mec.2020.e00133**.

75 S. C. Kim, D. J. Sukovich and A. R. Abate, Patterning Microfluidic Device Wettability with Spatially-Controlled Plasma Oxidation, *Lab Chip*, 2015, **15**(15), 3163–3169, DOI: **10.1039/C5LC00626K**.

76 N. J. Alvarez, L. M. Walker and S. L. Anna, A Non-Gradient Based Algorithm for the Determination of Surface Tension from a Pendant Drop: Application to Low Bond Number Drop Shapes, *J. Colloid Interface Sci.*, 2009, **333**(2), 557–562, DOI: **10.1016/j.jcis.2009.01.074**.

